ACS MATERIALS LETTERS

www.acsmaterialsletters.org

LETTER

Unraveling Piezoelectricity of Two-Dimensional Ferroelectric Metal 1T′′-MoS_2

Haidong Lu, Hugo Aramberri, Alexey Lipatov, Roger Proksch, Alexander Sinitskii,* Jorge Íñiguez,* and Alexei Gruverman*

Cite This: *ACS Materials Lett.* 2023, 5, 3136–3141

Read Online

ACCESS | Metrics & More | Article Recommendations

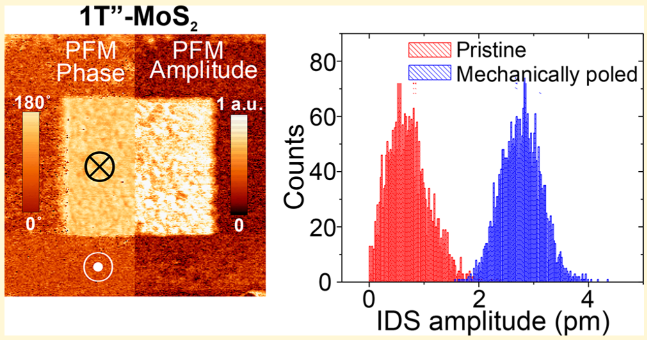

ABSTRACT: **The recent discovery of ferroelectric behavior in two-dimensional (2D) van der Waals materials has spurred interest in their piezoelectric properties, which are determined by the relative strength of the inter- and intralayer interactions. However, progress in this field is hindered by the high electrical conductivity and weak piezoelectricity of 2D ferroelectrics: establishing not only a magnitude but also a sign of the piezoelectric coefficient in these materials via measurements of the electrically induced strain as a function of polarization proved to be extremely challenging. Here, we report investigation of the longitudinal piezoelectric coefficient in the recently discovered 2D ferroelectric 1T′′-MoS_2 by means of local probe microscopy techniques. The electromechanical response and the surface potential of the flexoelectrically poled 1T′′-MoS_2 have been tested by piezoresponse and Kelvin probe force microscopies, respectively. The comparative interferometric displacement spectroscopy studies provide solid evidence of the mechanically induced polarization direction in 1T′′-MoS_2 and allow quantification of its piezoelectric response. It is found that 1T′′-MoS_2 exhibits negative piezoelectricity with a d_{33} value of the order of −3 pm/V. First-principles density-functional theory calculations support the experimental findings for d_{33} in both sign and magnitude.**

Over the last several years there has been a surge in theoretical predictions and experimental demonstrations of the ferroelectric ordering in two-dimensional (2D) van der Waals (vdW) materials, such as MoS_2, SnTe, $CuInP_2S_6$, WTe_2, In_2Se_3, and $MoTe_2$,[1−6] which opened a rich playground for fundamental studies of this collective phenomenon in systems with reduced dimensionality. Extensive studies of the piezoelectric behavior of 2D materials have been driven by the expectations that their scalability, mechanical strength, and flexibility could offer significant advantages in fabricating integrated microelectromechanical systems with enhanced performance.[7] Among the main challenges in unraveling the unique functionality of 2D ferroelectrics is a need for better understanding and reliable control of their polarization-coupled electromechanical properties. This challenge stems from the high electrical conductance of 2D ferroelectrics, which precludes the use of conventional electric methods for polarization control. The sparse experimental data obtained so far revealed an interesting phenomenon: a large negative value of the longitudinal piezoelectric coefficient in the layered vdW ferroelectric $CuInP_2S_6$.[8] This property is presumably due to the imbalance between strong intralayer and weak interlayer bonds with different elastic compliances. Because of this asymmetry, the piezoelectric deformation tends to preferentially affect the softer interlayer bond length rather than the intralayer bond length, resulting in the negative longitudinal piezoelectricity. This behavior is in striking contrast to that of conventional ferroelectrics, where positive longitudinal piezoelectricity is typically the result of the uniform ion shift in a continuous lattice of strong covalent bonds. It is interesting to see whether such periodic variations of the elastic compliance characteristics of layered materials would cause negative piezoelectricity in other vdW ferroelectrics.

Recently, a direct experimental observation of a stable room-temperature out-of-plane polarization and its reversal in 2D MoS_2 - one of the most promising and robust 2D electronic

Received: September 7, 2023
Revised: October 19, 2023
Accepted: October 20, 2023
Published: October 26, 2023

materials - has been reported.[2] This breakthrough was achieved by applying mechanical pressure using the tip of a scanning probe microscope. Mechanical switching of polarization is facilitated by the tendency of all materials to polarize under a strain gradient, the effect known as flexoelectricity. Using the strain gradient generated by the tip, stable bidomain polarization states, which exhibit different piezoelectric activity, have been produced and visualized by means of piezoresponse force microscopy (PFM). However, while the ferroelectric nature of MoS_2 and polarization control by mechanical means have been decisively demonstrated, there remained ambiguity regarding its piezoelectric properties, namely the sign of the piezocoefficient. In this paper, we employ interferometric displacement sensor (IDS) PFM measurements in combination with the surface potential testing by Kelvin probe force microscopy (KPFM) to provide insights into the electromechanical properties of the ferroelectric allotrope of molybdenum disulfide, 1T′′-MoS_2. The obtained results are compared to the reference ferroelectric samples and supported by first-principles modeling. Our observations indicate that 1T′′-MoS_2 exhibits a negative longitudinal piezoelectric coefficient of about −3.0 pm/V and a negative flexoelectric coefficient.

The 1T′′-MoS_2 samples were prepared by the lithiation using *tert*-butyllithium of the multilayer 2H-MoS_2 flakes (Figure 1(a)), which in turn was produced by micro-

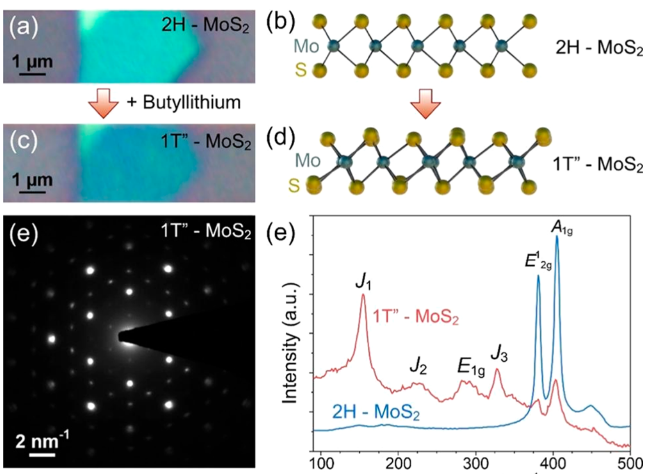

Figure 1. (a) Optical image of a mechanically exfoliated 2H-MoS_2 flake on the Si/SiO_2 substrate. (b) Side view of the crystal structure of 2H-MoS_2. (c) Optical image of the same flake after *tert*-butyllithium treatment. (d) Side view of the crystal structure of 1T′′-MoS_2. (e) Experimental SAED patterns of the MoS_2 flake after the lithiation treatment. (f) Raman spectra of the same MoS_2 flake before and after lithiation illustrating its transformation from the 2H to the 1T′′ phase.

mechanical exfoliation of naturally occurring bulk MoS_2 crystals, which crystallize in the hexagonal $P6_3/mmc$ space group (Figure 1(b)). Observation of the color change to a darker hue of the lithiated flake (Figure 1(c)) verifies the intended conversion to the 1T′′-MoS_2 phase (Figure 1(d)). The selected area electron diffraction (SAED) pattern of the exemplar MoS_2 flake after lithiation reveals a distinct diffraction pattern, which corresponds to the doubling of the unit cell parameters (Figure 1(e)), indicating the formation of the 1T″ phase with the ~$2a_o \times 2a_o$ superstructure, where a_o is the lattice parameter of 2H-MoS_2. The emergence of additional Raman peaks at 155, 225, 289, and 328 cm^{-1} corresponding to the J_1, J_2, E_{1g}, and J_3 modes of the 1T′′ phase (Figure 1(f)) further confirms the transition from the 2H to the 1T′′-MoS_2 phase. For the purposes of further experiments, the conversion of 2H-MoS_2 to 1T′′-MoS_2 was performed on Pt-covered Si/SiO_2 substrates.

In the mechanical switching approach, a sharp probing tip is pressed against the sample surface producing a highly nonuniform strain, which generates a flexoelectric field $E = f\frac{du}{dz}$ (where f is a flexocoupling coefficient and $\frac{du}{dz}$ is a strain gradient). In all the experimental studies on flexoelectric switching reported up to now,[9−13] the tip-induced pressure leads to the downward (pointing toward the bottom electrode) polarization state. However, in the absence of *a priori* known information about the flexoelectric coefficient sign, it is impossible to ascertain a direction of the mechanically switched polarization. Specifically, the polarization direction can be determined in PFM by monitoring the phase φ of the sample piezoelectric oscillations induced by a small AC drive voltage: $z = d_{33}V_{ac}\cos(\omega t + \varphi)$, provided that the sign of the piezoelectric coefficient d_{33} is known. The PFM approach also allows solving a reverse problem: if a polarization direction is somehow known (i.e., from the polarity of the applied switching voltage), then the sign of the piezoelectric coefficient can be obtained from the phase of the PFM signal: a ferroelectric polarized downward will oscillate in phase with the AC drive voltage if its piezocoefficient d_{33} is positive. However, if neither the polarization direction nor the piezoelectric coefficients are known, then a reliable interpretation of the measured PFM signal becomes unfeasible.

To address this uncertainty with respect to the mechanical switching in 1T′′-MoS_2, we employ KPFM as a more direct way of testing the surface charges associated with polarization and compare the obtained results with a reference ferroelectric material - $BaTiO_3$ thin film. Figure 2 shows the PFM and KPFM images of the $BaTiO_3$ thin film (Figure 2(a,b)) and 1T′′-MoS_2 flake (Figure 2(c,d)) where mechanical poling was

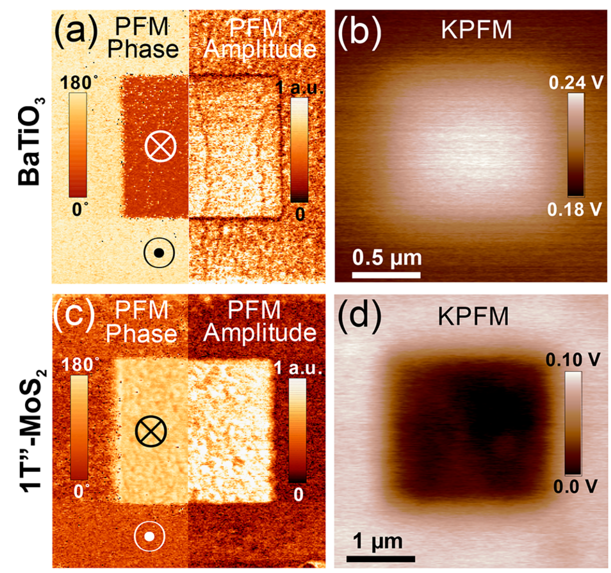

Figure 2. (a,c) PFM amplitude and phase and (b,d) KPFM images of the mechanically poled $BaTiO_3$ thin film (a,b) and 1T′′-MoS_2 flake (c,d).

https://doi.org/10.1021/acsmaterialslett.3c01051
ACS Materials Lett. 2023, 5, 3136−3141

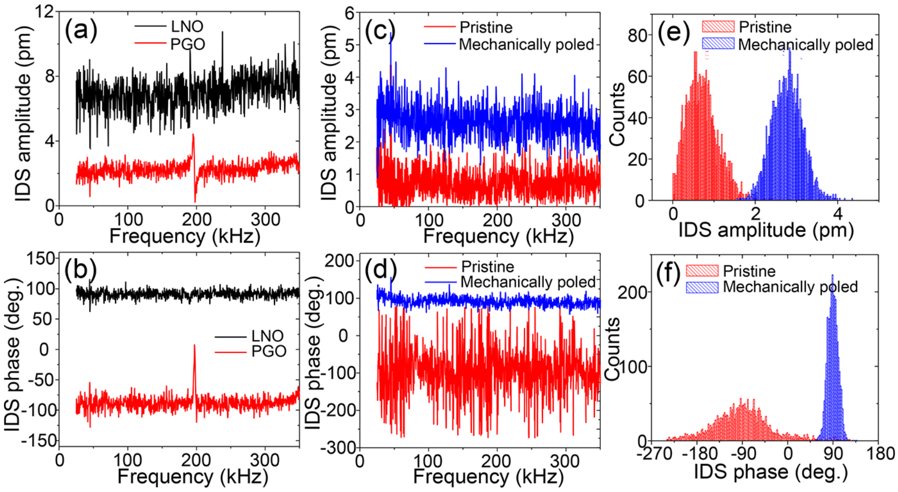

Figure 3. IDS measurements of the reference samples of lithium niobate $LiNbO_3$ (LNO) and lead germanate $Pb_5Ge_3O_{11}$ (PGO) and of 1T′′-MoS_2. (a,b) IDS amplitude and phase signals obtained in the LNO sample with the *upward* polarization and in the PGO sample with the *downward* polarization. (c,d) IDS amplitude (c) and phase (d) signals measured in the pristine and mechanically poled 1T′′-MoS_2. (e,f) Histograms of the IDS signals shown in (c) and (d). The AC drive used for all measurements is 1 V.

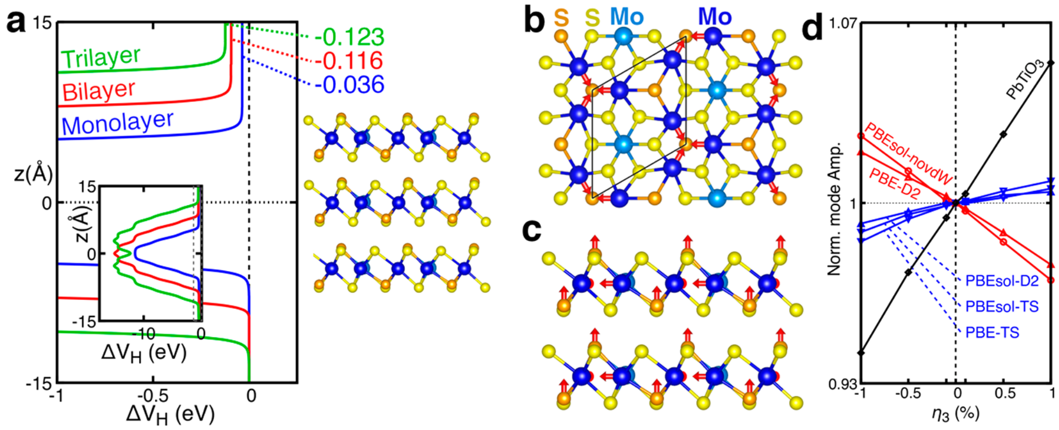

Figure 4. Summary of the DFT calculations. (a) Results for the Hartree potential difference $\Delta V_H = V_H(z) - V_H(-\infty)$ as a function of the distance to the slab for the slabs of different thicknesses. These results are obtained with PBEsol using the Tkatchenko-Scheffler method for the vdW interactions (see the Experimental Section). Blue, red, and green lines correspond to monolayer, bilayer, and trilayer slabs schematically shown to the right. The inset shows the same data for ΔV_H when zooming out the potential energy scale. (b) Top and (c) side views of the simulation cell of bulk 1T″-MoS_2, with red arrows indicating the polar distortion of symmetry Γ_2^-. At equilibrium, this polar distortion corresponds to a polarization $P_3 = 6 \times 10^{-4}$ C/m^2. (d) Relative change in polar distortion (and thus in polarization) as a function of longitudinal strain η_3 applied to the bulk system. The shown results are obtained for several approximations to DFT (see the Experimental Section). The results in blue correspond to a positive e_{33} coefficient with the largest value of about +0.05 C/m^2. The results in red correspond to a negative e_{33} coefficient with the largest value of about −0.18 C/m^2. The black line shows the results for ferroelectric perovskite $PbTiO_3$ with e_{33} = +1.62 C/m^2.

performed by scanning an area of several square microns with the PFM tip under an applied load of 1100 nN. Inversion of the PFM phase contrast by 180° is an indication of the polarization reversal by the tip-induced mechanical stress, which is also accompanied by the change in the KFPM signal. Remarkably, the observed changes are opposite in $BaTiO_3$ and 1T′′-MoS_2. In particular, the KPFM image of 1T′′-MoS_2 (Figure 2(d)) shows a decreased surface potential in the mechanically poled region, while in $BaTiO_3$, the KPFM signal increases (Figure 2(b,d)). It has been well-established[9] that the tip-induced flexoelectric switching in $BaTiO_3$ produces a downward polarization state. Hence, the enhanced KPFM signal after mechanical poling could be related to the accumulation of the positive screening charges on the $BaTiO_3$ surface. However, in the case of 1T′′-MoS_2 with its weak polarization and metallic behavior, it is likely that surface screening of polarization is less pronounced if present at all. Consequently, we conclude that in 1T′′-MoS_2, KPFM detects a signal related to the bound polarization charges; hence, a decrease of the surface potential observed in the mechanically poled 1T′′-MoS_2 should be an indication of the negative bound charges. Thus, similar to $BaTiO_3$, the tip-induced pressure generates a downward polarization in 1T′′-MoS_2 indicating a negative flexoelectric coefficient in this material.

To obtain further insight, we employed IDS PFM spectroscopy to perform quantitative measurements of the piezoelectric response of the mechanically poled 1T′′-MoS_2. The IDS PFM approach is based on direct sensing of the cantilever displacement by means of the laser Doppler effect, which eliminates parasitic contributions to the electromechanical

https://doi.org/10.1021/acsmaterialslett.3c01051
ACS Materials Lett. 2023, 5, 3136−3141

signal associated with complex cantilever dynamics.[14] Figure 3 shows the IDS amplitude and phase signals as a function of the AC drive frequency measured in two reference samples: single crystals of uniaxial ferroelectrics lithium niobate $LiNbO_3$ (LNO) and lead germanate $Pb_5Ge_3O_{11}$ (PGO). The magnitude of the effective d_{33} coefficient is calculated to be 7 pm/V for LNO and 2 pm/V for PGO. These two crystals are used as a reference for the calibration of the IDS signal (the signs and magnitudes of the piezoelectric coefficients in these materials have been determined by independent methods[15−17]). The IDS phase signal is stable throughout the measurement frequency range and gives an output of +90° (relative to the AC drive signal) for LNO (which is in the *upward* polarization state) and −90° for PGO (which is in the *downward* polarization state). An internal phase offset of −90° of the lock-in amplifier causes the specific values of the measured phase signals (subtraction of the offset would yield a phase of 180° for the out-of-phase signal and 0° for the in-phase signal, respectively). Note that both materials exhibit positive longitudinal piezoelectricity.

The IDS measurement results for pristine and mechanically poled 1T′′-MoS_2 are shown in Figure 3(c,e). A histogram analysis of the IDS amplitude data (Figure 3(e)) reveals a low effective d_{33} of 0.7 ± 0.4 pm/V in the pristine state (which is slightly above the noise level of 0.5 pm/V) but a much higher d_{33} value of 2.8 ± 0.4 pm/V in the mechanically poled state. As for the IDS phase signal (Figure 3(d,f)), the pristine 1T′′-MoS_2 sample shows a fairly noisy signal with a wide distribution centering at −90° (Figure 3(f)) due to the fact that the amplitude signal is approaching the noise level. On the other hand, mechanically poled 1T′′-MoS_2 shows a much more stable frequency-independent signal with a narrow distribution centered at +90°. The fact that 1T″-MoS_2, mechanically poled to the downward polarization state, exhibits the IDS phase of +90° with respect to the AC drive signal implies a negative sign of the longitudinal piezoelectric coefficient in this material.

We now turn to first-principles density-functional theory (DFT) calculations to study the longitudinal piezoresponse of 1T″-MoS_2. First, to build confidence in our computational approach, we study an isolated slab with the polarization pointing up and compute the Hartree potential $\Delta V_H(z) = V_H(z) - V_H(-\infty)$, where z is the distance to the center of the slab. As shown in Figure 4(a), the Hartree potential converges to $\Delta V_H\ (z \to \infty) \approx -0.12$ eV as the slab thickness increases. Its negative sign indicates the preference of the top surface to attract electrons, as expected. The calculated potential difference is in agreement with the KPFM measurements of the poled and unpoled regions, which yield a value on the order of 0.1 V (Figure 2(d)), suggesting a one-to-one correspondence between the simulations and the experimental results.

To compute the piezoelectric response, we use the periodic boundary conditions in the bulk-limit of the MoS_2 multilayer, as sketched in Figure 4(b,c). The interlayer spacing can be reliably obtained from first-principles calculations using various well-known flavors of DFT and corrections to incorporate the vdW forces (see the Experimental Section). However, the quantification of the electric polarization in the bulk limit is problematic: we obtain a metallic solution regardless of the DFT approximations involved, and in such a scenario, the static equilibrium polarization is not well-defined. Nevertheless, as detailed in the Experimental Section, we know that the polarization of 1T″-MoS_2 is proportional to a particular structural distortion of polar Γ_2^- symmetry (Figure 4(b,c)). Further, we can readily quantify the dependence of such a polar distortion on the out-of-plane strain η_3 and thus estimate the longitudinal piezoelectric coefficient e_{33}.

The obtained results are listed in Figure 4(d). We find that different approximations to DFT and the vdW couplings result in e_{33} responses of a different sign, with values ranging between +0.05 and −0.18 C/m^2. Noting that the employed approximations are generally reliable and consistent, this suggests that the piezoelectric response - which involves subtle variations in the interlayer couplings caused by small changes in the polar distortion - is a very challenging quantity to compute from the first principles. This conclusion is consistent with the relatively small magnitude of $|e_{33}|$ that our calculations yield. For comparison, the e_{33} for prototype ferroelectric perovskite $PbTiO_3$ is predicted to be about +1.62 C/m^2 (i.e., about 10 times bigger) (Figure 4(d)).

Interestingly, the longitudinal elastic constant C_{33} of bulk 1T″-MoS_2 computed from DFT is about 74 GPa. This relatively small value is a result of the elastic softness of the MoS_2 multilayer along the stacking direction (due to the relatively weak vdW forces). Noting that $d_{33} \approx e_{33}/C_{33}$, our calculations suggest that the longitudinal piezoresponse lies somewhere between −2.4 and 0.7 pm/V. Hence, the DFT results are not incompatible with the experimental observations. Indeed, our calculations seem to lean toward a negative longitudinal piezoelectric effect of a magnitude that is very similar to the experimentally measured value of −2.8 ± 0.4 pm/V (see above). Note that due to the subtlety of the effect and the difficulty to quantify it from the first-principles, it is not presently feasible to discuss its physical origin of negative piezoelectricity of 1T″-MoS_2. This issue needs to be addressed in future studies similar to the recently published report.[18]

In summary, scanning probe microscopy methods have been used to determine the sign of the longitudinal piezoelectric coefficient d_{33} of 2D ferroelectric metal 1T′′-MoS_2 and to measure its magnitude. Comparative analysis of information obtained from the KPFM and IDS PFM measurements of the mechanically poled 1T′′-MoS_2 and reference ferroelectric samples reveals negative piezoelectricity of 1T′′-MoS_2, similar to other 2D vdW ferroelectrics. The first-principles calculations carried out using different computational approaches yield a range of the d_{33} values of both positive and negative signs but lean toward a negative longitudinal piezocoefficient with a magnitude consistent with the experimentally measured one.

■ EXPERIMENTAL SECTION

Sample Preparation. 2H-MoS_2 flakes with thicknesses ranging from 5 to 20 nm were exfoliated from commercial MoS_2 crystals (SPI supplies) using an adhesive tape and deposited on conductive ($Pt/SiO_2/Si$) substrates. The samples were soaked in dry hexane for 5 min and then in a 2.5 M solution of *tert*-butyllithium in hexane for 3 h. The produced 1T′′-MoS_2 flakes were then soaked in dry hexane and rinsed with ethanol to remove possible lithium residues. Optical microscopy was conducted to locate flakes with uniform colors and clean surfaces, which were used for further studies. Details of sample preparation can be found in ref 2.

Structural Characterization. Raman spectra of the pristine and lithiated MoS_2 flakes were recorded by using a Thermo Scientific DXR Raman microscope with a 532 nm excitation laser. A relatively low laser power of 2 mW was used

https://doi.org/10.1021/acsmaterialslett.3c01051
ACS Materials Lett. 2023, 5, 3136−3141

to prevent possible phase transformations in MoS_2 flakes due to overheating. The SAED diffraction pattern of the $1T''$-MoS_2 flake was recorded using a FEI Tecnai Osiris scanning transmission electron microscope (TEM) equipped with an HAADF detector and an X-FEG high brightness Schottky field emission gun; the accelerating voltage was 200 kV. The flake was transferred from the SiO_2/Si substrates to a TEM grid using a sacrificial cellulose film.

IDS Measurements. The IDS measurements were performed on an AFM system (Cypher, Asylum Research) equipped with an IDS setup. Pt-coated conductive probes (PPP-EFM, Nanosensors) were used for the measurement of piezoresponse. An AC amplitude of 1 V was used for the AC drive. A frequency sweep of the AC voltage was applied to the sample surface via the conductive probe, and the piezoresponse deformation was picked up by the PFM probe and detected by the IDS setup.

KPFM and PFM Measurements. The KPFM and PFM measurements were performed on an AFM system (MFP-3D, Asylum Research) using conductive probes (PPP-EFM, Nanosensors). Mechanical poling was done by scanning an area at a 1.1 μN load with a grounded probe, and PFM was done in the resonant enhanced mode with an AC drive of 0.5 V around 350 kHz.

First-Principles Calculations. Density functional theory calculations were performed as implemented in the Vienna Ab Initio simulation package (VASP).[19,20] We employ the projector-augmented wave approach[21] for the pseudopotentials, solving explicitly for the following electrons: 4*s*, 4*p*, 4*d* and 5*s* for Mo; 3*s* and 3*p* for S; 5*d*, 6*s*, and 6*p* for Pb; 3*p*, 4*s*, and 3*d* for Ti; and 2*s* and 2*p* for O. We employ a plane-wave energy cutoff of 500 eV, which we found to yield converged results. We use a 7 × 7 × 1 k-point mesh for the slab calculations and an 8 × 8 × 8Monkhorst−Pack[22] grid for the bulk calculations. The Perdew−Burke−Ernzerhof (PBE)[23] implementation of the generalized gradient approximation and its modified version for solids (PBEsol)[24] are used for the exchange-correlation functional. We consider different types of implementations for the vdW interactions: the semiempirical method of Grimme (D2),[25] the Tkatchenko-Scheffler approach[26] (TS), and no vdW corrections (novdW). In slab calculations, we use the standard dipole corrections among image slabs to achieve a vanishing electric field in vacuum.[27] Structural optimizations were carried out until atomic forces fell below 0.1 eV Å^{-1} and the total stress fell below 1 MPa. Different combinations of exchange functionals and vdW corrections yield different out-of-plane lattice parameters for the bulk 1T″ phase, ranging from 5.60 Å (PBEsol+D2) to 6.63 Å (PBE, no vdW correction). We also employ the visualization software VESTA[28] for the structural representations.

Since bulk $1T''$-MoS_2 is metallic, we cannot employ the standard methods - based on the Berry-phase theory of polarization[29] - to calculate its polarization and piezoelectric response. (For a discussion of when and how the Berry phase theory can be applied in the context of ferroelectric metals with very anisotropic conductivity (1D or 2D), see ref 30. Note, however, that $1T''$-MoS_2 is a 3D metal, so it is beyond the scope of the Berry phase approach.) Instead, following the approach in ref 2, we resort to calculations with finite slabs to quantify the associated electric dipole, which can be obtained from the electronic charge density (and ionic positions) in real space. After suitable normalization by the volume of the bulk unit cell, we estimate $P_3 = 6 \times 10^{-4}$ C/m^2 at equilibrium. We then focus on the polar distortion responsible for this polarization, which has a specific symmetry (Γ_2^-) and whose amplitude can be quantified (with respect to a suitable high-symmetry reference structure to which we assign $P_3 = 0$) using the standard crystallographic tool ISODISTORT.[31] Then, by computing this amplitude as a function of the imposed strain η_3, we can quantify the piezoelectric coefficient e_{33}.

■ AUTHOR INFORMATION

Corresponding Authors

Alexander Sinitskii − *Department of Chemistry, University of Nebraska, Lincoln, Nebraska 68588, United States;* orcid.org/0000-0002-8688-3451; Email: sinitskii@unl.edu

Jorge Íñiguez − *Department of Materials Research and Technology, Luxembourg Institute of Science and Technology, L-4362 Esch/Alzette, Luxembourg; Department of Physics and Materials Science, University of Luxembourg, L-4422 Belvaux, Luxembourg;* orcid.org/0000-0001-6435-3604; Email: jorge.iniguez@list.lu

Alexei Gruverman − *Department of Physics and Astronomy, University of Nebraska, Lincoln, Nebraska 68588, United States;* orcid.org/0000-0003-0492-2750; Email: agruverman2@unl.edu

Authors

Haidong Lu − *Department of Physics and Astronomy, University of Nebraska, Lincoln, Nebraska 68588, United States*

Hugo Aramberri − *Department of Materials Research and Technology, Luxembourg Institute of Science and Technology, L-4362 Esch/Alzette, Luxembourg;* orcid.org/0000-0003-2216-8931

Alexey Lipatov − *Department of Chemistry, University of Nebraska, Lincoln, Nebraska 68588, United States;* orcid.org/0000-0001-5043-1616

Roger Proksch − *Asylum Research an Oxford Instruments Company, Santa Barbara, California 93117, United States;* orcid.org/0000-0003-2124-1201

Complete contact information is available at: https://pubs.acs.org/10.1021/acsmaterialslett.3c01051

Notes

The authors declare no competing financial interest.

■ ACKNOWLEDGMENTS

Research at the University of Nebraska was supported by the National Science Foundation (NSF) under Grant DMR-2212965 (A.G.), NSF EPSCoR RII Track-1: Emergent Quantum Materials and Technologies (EQUATE) Award OIA-2044049 (A.S.), and NSF Award OIA-2329159 (A.L.). Sample characterization was performed using the instrumentation at the Nebraska Nanoscale Facility supported by the National Science Foundation (ECCS-2025298) and the Nebraska Research Initiative. Work at LIST was supported by the Luxembourg National Research Fund (FNR) through Grant No. C21/MS/15799044/FERRODYNAMICS.

■ REFERENCES

(1) Shirodkar, S. N.; Waghmare, U. V. Emergence of Ferroelectricity at a Metal-Semiconductor Transition in a 1T Monolayer of MoS_2. *Phys. Rev. Lett.* **2014**, *112*, No. 157601.

(2) Lipatov, A.; Chaudhary, P.; Guan, Z.; Lu, H.; Li, G.; Crégut, O.; Dorkenoo, K. D.; Proksch, R.; Cherifi-Hertel, S.; Shao, D. F.; Tsymbal, E. Y.; Íñiguez, J.; Sinitskii, A.; Gruverman, A. Direct Observation of Ferroelectricity in Two-Dimensional MoS_2. *npj 2D Mater. Appl.* **2022**, *6*, 18.

(3) Xiao, J.; Zhu, H.; Wang, Y.; Feng, W.; Hu, Y.; Dasgupta, A.; Han, Y.; Wang, Y.; Muller, D. A.; Martin, L. W.; Hu, P. A.; Zhang, X. Intrinsic two-dimensional ferroelectricity with dipole locking. *Phys. Rev. Lett.* **2018**, *120*, No. 227601.

(4) Yuan, S.; Luo, X.; Chan, H. L.; Xiao, C.; Dai, Y.; Xie, M.; Hao, J. Room-temperature ferroelectricity in $MoTe_2$ down to the atomic monolayer limit. *Nat. Commun.* **2019**, *10*, 1775.

(5) Liu, F.; You, L.; Seyler, K. L.; Li, X.; Yu, P.; Lin, J.; Wang, X.; Zhou, J.; Wang, H.; He, H.; Pantelides, S. T.; Zhou, W.; Sharma, P.; Xu, X.; Ajayan, P. M.; Wang, J.; Liu, Z. Room-temperature ferroelectricity in $CuInP_2S_6$ ultrathin flakes. *Nat. Commun.* **2016**, *7*, 12357.

(6) Guan, Z.; Hu, H.; Shen, X.; Xiang, P.; Zhong, N.; Chu, J.; Duan, C. Recent Progress in Two-Dimensional Ferroelectric Materials. *Adv. Electron. Mater.* **2020**, *6*, No. 1900818.

(7) Chen, S.-B.; Zeng, Z.-Y.; Chen, X.-R.; Yao, X.-X. Strain-induced electronic structures, mechanical anisotropy, and piezoelectricity of transition-metal dichalcogenide monolayer CrS_2. *J. Appl. Phys.* **2020**, *128*, No. 125111.

(8) You, L.; Zhang, Y.; Zhou, S.; Chaturvedi, A.; Morris, S. A.; Liu, F.; Chang, L.; Ichinose, D.; Funakubo, H.; Hu, W.; Wu, T.; Liu, Z.; Dong, S.; Wang, J. Origin of giant negative piezoelectricity in a layered van der Waals ferroelectric. *Sci. Adv.* **2019**, *5*, No. eaav3780.

(9) Lu, H.; Bark, C.-W.; Esque de los Ojos, D.; Alcala, J.; Eom, C. B.; Catalan, G.; Gruverman, A. Mechanical writing of ferroelectric polarization. *Science* **2012**, *336*, 59−61.

(10) Sharma, P.; Ryu, S.; Viskadourakis, Z.; Paudel, T. R.; Lee, H.; Panagopoulos, C.; Tsymbal, E. Y.; Eom, C. B.; Gruverman, A. Electromechanics of ferroelectric-like behavior of LaAlO3 thin films. *Adv. Funct. Mater.* **2015**, *25*, 6538−6544.

(11) Chen, X.; Tang, X.; Chen, X.-Z.; Chen, Y.-L.; Guo, X.; Ge, H.-X.; Shen, Q.-D. Nonvolatile data storage using mechanical force-induced polarization switching in ferro- electric polymer. *Appl. Phys. Lett.* **2015**, *106*, No. 042903.

(12) Park, S. M.; Wang, B.; Das, S.; Chae, S. C.; Chung, J.-S.; Yoon, J.-G.; Chen, L.-Q.; Yang, S. M.; Noh, T. W. Selective control of multiple ferroelectric switching pathways using a trailing flexoelectric field. *Nat. Nanotechnol.* **2018**, *13*, 366−370.

(13) Guan, Z.; Li, Y.-K.; Zhao, Y.-F.; Peng, Y.; Han, G.; Zhong, N.; Xiang, P.-H.; Chu, J.-H.; Duan, C.-G. Mechanical Polarization Switching in $Hf_{0.5}Zr_{0.5}O_2$ Thin Film. *Nano Lett.* **2022**, *22*, 4792−4799.

(14) Labuda, A.; Proksch, R. Quantitative measurements of electromechanical response with a combined optical beam and interferometric atomic force microscope. *Appl. Phys. Lett.* **2015**, *106*, No. 253103.

(15) Smith, R. T.; Welsh, F. S. Temperature Dependence of the Elastic, Piezoelectric, and Dielectric Constants of Lithium Tantalate and Lithium Niobate. *J. Appl. Phys.* **1971**, *42*, 2219−2230.

(16) Jazbinšek, M.; Zgonik, M. Material tensor parameters of $LiNbO_3$ relevant for electro- and elasto-optics. *Appl. Phys. B: Laser Opt.* **2002**, *74*, 407−414.

(17) Yamada, T.; Iwasaki, H.; Niizeki, N. Elastic and Piezoelectric Properties of Ferroelectric $5PbO \cdot 3GeO_2$ Crystals. *J. Appl. Phys.* **1972**, *43*, 771−775.

(18) Arora, A.; Rawat, R.; De Sarkar, A. Negative piezoelectricity and enhanced electrical conductivity at the interfaces of two-dimensional dialkali oxide and chalcogenide monolayers. *Phys. Rev. B* **2023**, *107*, No. 085402.

(19) Kresse, G.; Furthmüller, J. Efficient iterative schemes for *ab initio* total-energy calculations using a plane-wave basis set. *Phys. Rev. B* **1996**, *54*, 11169.

(20) Kresse, G.; Joubert, D. From Ultrasoft Pseudopotentials to the Projector Augmented-Wave Method. *Phys. Rev. B* **1999**, *59*, 1758.

(21) Blöchl, P. E. Projector augmented-wave method. *Phys. Rev. B* **1994**, *50*, 17953.

(22) Monkhorst, H. J.; Pack, J. D. Special Points for Brillouin-Zone Integrations. *Phys. Rev. B* **1976**, *13*, 5188.

(23) Perdew, J. P.; Burke, K.; Ernzerhof, M. Generalized Gradient Approximation Made Simple. *Phys. Rev. Lett.* **1996**, *77*, 3865.

(24) Perdew, J. P.; Ruzsinszky, A.; Csonka, G. I.; Vydrov, O. A.; Scuseria, G. E.; Constantin, L. A.; Zhou, X.; Burke, K. Restoring the Density-Gradient Expansion for Exchange in Solids and Surfaces. *Phys. Rev. Lett.* **2008**, *100*, No. 136406.

(25) Grimme, S. Semiempirical GGA-type density functional constructed with a long-range dispersion correction. *J. Comput. Chem.* **2006**, *27*, 1787.

(26) Tkatchenko, A.; Scheffler, M. Accurate Molecular Van Der Waals Interactions from Ground-State Electron Density and Free-Atom Reference Data. *Phys. Rev. Lett.* **2009**, *102*, No. 073005.

(27) Bengtsson, L. Dipole correction for surface supercell calculations. *Phys. Rev. B* **1999**, *59*, 12301.

(28) Momma, K.; Izumi, F. VESTA 3 for three-dimensional visualization of crystal, volumetric and morphology data. *J. Appl. Crystallogr.* **2011**, *44*, 1272−1276.

(29) King-Smith, R. D.; Vanderbilt, D. Theory of polarization of crystalline solids. *Phys. Rev. B* **1993**, *47*, 1651.

(30) Filippetti, A.; Fiorentini, V.; Ricci, F.; Delugas, P.; Íñiguez, J. Prediction of a native ferroelectric metal. *Nat. Commun.* **2016**, *7*, 11211.

(31) Campbell, B. J.; Stokes, H. T.; Tanner, D. E.; Hatch, D. M. ISODISPLACE: a web-based tool for exploring structural distortions. *J. Appl. Crystallogr.* **2006**, *39*, 607−614.

https://doi.org/10.1021/acsmaterialslett.3c01051
ACS Materials Lett. 2023, 5, 3136−3141